Int. J. Solids Structures Vol. 21, No. 8, pp. 865–888, 1985
Printed in Great Britain.

0020–7683/85 $3.00 + .00
Pergamon Press Ltd.

QUASI-STATIC NORMAL INDENTATION OF AN ELASTO-PLASTIC HALF-SPACE BY A RIGID SPHERE—II. RESULTS

G. B. SINCLAIR
Department of Mechanical Engineering, Carnegie-Mellon University, Pittsburgh, PA 15213, U.S.A.

P. S. FOLLANSBEE
Group CMB-5 MS 730, Los Alamos National Laboratories, Los Alamos, NM 87545, U.S.A.

and

K. L. JOHNSON
Cambridge University Engineering Department, Trumpington St., Cambridge CB2 1PZ, U.K.

(*Received* 26 *March* 1984; *in revised form* 25 *September* 1984)

Abstract—The title problem is considered within the theory of incremental elastoplasticity and results of an earlier finite element analysis (Part I) processed to furnish: the indentation response with increasing pressure, contact and interior stresses on loading and unloading, yield region growth, strain distributions, and surface displacement profiles. The more significant findings stemming from these results may be summarized as being: theoretical confirmation of Tabor's simple experimental correlations for work-hardening materials, demonstration of an improved finite element capability, over that reported previously in terms of accuracy and ability to track the indentation processes to higher load levels, an appreciation of some of the inadequacies of slip-line analysis in dealing with problems of this type, generally good agreement between theory and the physical evidence whenever comparison possible, nearly self-similar response to increasing load in the fully plastic regime, and some quantification of the residual tensile stresses that can occur.

INTRODUCTION

The contact problem considered here seeks the stresses and deformations that accumulate when a sphere is slowly pressed normally into a relatively soft half-space. This configuration has implications for a variety of engineering situations, such as the Brinell hardness test. As a result, it has attracted the attention of a number of investigators (see Johnson[1] for a recent review), the contributions including the analysis within the theory of incremental elasto-plasticity that constitutes the first part of this study, Follansbee and Sinclair[2]. In [2], a simple but effective finite element technique is described which apparently enables the analysis to be taken forward to the upper load levels encountered in practice while still retaining the requisite accuracy to determine the quantities of physical import: here the intent is to furnish a summary and discussion of the *extensive results* provided by such an exercise. In particular, the objective is to *compare* results found, first and foremost *with companion physical* ones and secondly with those of *other analyses*.

We begin in Section 1 by briefly restating the problem and outlining the procedures employed to reduce the numerical data attending its finite element analysis (an assessment of accompanying numerical noise is given in an Appendix). Thereafter, in Section 2, we present results for the indentation extent versus pressure, and the stresses, strains, and displacements at different load levels.

1. PROBLEM DESCRIPTION: DATA PROCESSING

Here we first give, for completeness, an abbreviated formulation of the problem and a short account of its finite element analysis.† Next, we describe the means used

---

† For a more precise mathematical formulation and details of the analysis, see [2].

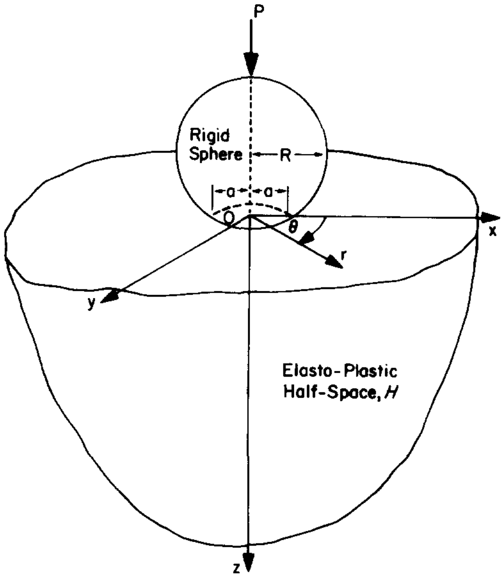

Fig. 1. Configuration and coordinates.

to reduce and smooth the plethora of data stemming from this analysis, then conclude with the measure adopted to monitor the numerical noise present prior to such smoothing.

To position the geometry entailed we let (x, y, z) be rectangular cartesian coordinates with origin O such that the surface of the *half-space* H is formed by the xy-plane with z positive into H (Fig. 1), and take (r, θ, z) as cylindrical polar coordinates related to the rectangular by

$$x = r\cos\theta,\ y = r\sin\theta,\ z = z (0 \leq r < \infty,\ 0 \leq \theta < 2\pi,\ -\infty < z < \infty). \quad (1.1)$$

Accordingly,

$$H = \{(r, \theta, z)\ |\ 0 \leq r < \infty,\ 0 \leq \theta < 2\pi,\ 0 < z < \infty\}. \quad (1.2)$$

Initially, the half-space is undisturbed; at some subsequent time, a *rigid sphere* of radius R is pressed normally into the half-space by a *load* P to the extent that contact occurs on a circle centered on O having radius a. We seek then, the *axisymmetric stresses* $\boldsymbol{\sigma} = (\sigma_r, \sigma_\theta, \sigma_z, \tau_{rz})$, *strains* $\boldsymbol{\epsilon} = (\epsilon_r, \epsilon_\theta, \epsilon_z, \gamma_{rz})$, and *displacements* $\mathbf{u} = (u, w)$, as functions of r, z throughout H for all time, resuting from the accumulation of their corresponding rates, which are to satisfy the following requirements:‡ the stress-rate equations of *equilibrium*; the *flow rule* for a homogeneous and isotropic, elastic/incompressible-plastic solid complying with von Mises' yield criterion; the *strain-rate/displacement-rate* relations for small strain rates; the *contact conditions* which prescribe vertical displacement increments consistent with indentation by a rigid sphere in conjunction with either complete constraint of transverse displacement increments to simulate *adhesive* contact or the shear stress rate set to zero to model *frictionless* contact; the stress-rate conditions on the remainder of the half-space surface that maintain a *free* boundary there; and, finally, the displacement-rate *conditions at infinity* which are such that the displacements continue to be zero there.

The preceding problem statement is quite general, in so far as the material comprising the half-space is concerned; for finite element analysis, however, further specifics of the flow rule must be given with a definite *stress-strain curve* prescribed. The material curve chosen in the ensuing treatment is that of 304L stainless steel (Fig. 2)

---

‡ The usual notation for the stress and strain components applies and u, w are the displacements in the r, z directions, respectively.

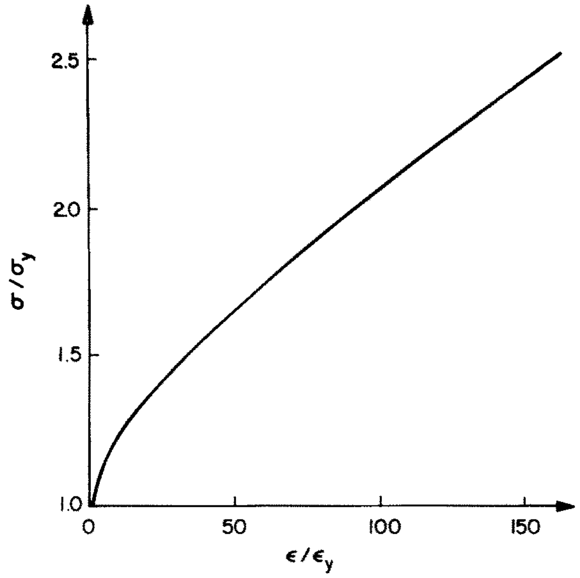

Fig. 2. Uniaxial stress (σ) versus strain (ϵ) hardening curve.

which has:§

$$E = 28 \times 10^3\text{ksi}\ (193 \times 10^3\text{MPa}),\ \nu = 0.28,\ \sigma_y = 35.2\text{ksi}\ (243\text{MPa}), \qquad (1.3)$$

where E is Young's modulus, ν Poisson's ratio, and $\sigma_y(\epsilon_y)$ is the uniaxial yield stress (strain). Although no single work-hardening or strain-hardening exponent n is available to characterize the material response throughout the range displayed in Fig. 2 (*cf.*, Ludwigson[4]), it is evident that the curve reflects appreciable work hardening and simple fits have n rising from an initial value of about 0.15 to a value ultimately approaching 0.5. As a consequence, we can expect the material selected to be capable of demonstrating the differences between indenting a material which strain hardens and indenting one which does not, *i.e.*, a perfectly plastic material with $n = 0$.

Using the actual material data contained in effect in (1.3) and Fig. 2, application of the *finite element method* (FEM) to the problem proceeds routinely, with discretization being limited to a plane circular quadrant by virtue of the axisymmetry, and the finite radius of the quarter-circle, which is set at the outset so as to model an infinite quarter-plane, being rescaled periodically to improve the resolution of the grid as indentation increases. To further improve resolution, the element preferred for use in this problem, the constant-stress triangle, is reduced in size near the contact area. Unfortunately, this element gradation makes it almost impossible to orientate all the triangular elements in the same manner. Hence a given *element* does not see the same pattern of other elements in all directions, and it is thought that this artificial numerical anisotropy is responsible, at least in part, for the introduction of spurious element-to-element fluctuations as indentation/computation progresses. With some 5000-odd steps requiring computation to apply the loads desired here, these oscillations can attain quite undesirable amplitudes. Fortunately, the gradated element map can be constructed so that the *nodes* sit with quasi-isotropic views of their surroundings, and it is, therefore, to be expected that, with such a grid, the nodal values would accrue less of this type of numerical noise. This is indeed found to be true, and thus throughout this study all results reported stem from *nodal values*, these being computed directly in the case of displacements or as simple averages of the values for the elements in common in the instance of stresses or strains.

---

§ The reason for this particular choice was to allow the direct experimental comparison of [2]. Other materials analyzed included Cu and Cu-7.5Al. Unfortunately, these analyses were undertaken to a somewhat different end than the present, and no close check was kept on the indentation extent, so that an objective full comparison of the results found with those to be given here is difficult—the results are qualitatively very similar, though (see Follansbee[3]).

By and large, these nodal values can be used directly to present results; for the contact stresses, though, no full cluster of elements encircles the surface nodes, so that it is not clear exactly what a simple element average there represents. Consequently, we drop down from these points of ambiguity to near-surface *interior* nodes that are completely enclosed in elements and extrapolate the associated nodal values up to the surface, the extrapolation used depending upon the contact condition being enforced. For the frictionless condition, the absence of shear stresses on the surface insists, via equilibrium, that

$$\frac{\partial \sigma_z}{\partial z} = 0 \text{ at } z = 0, \tag{1.4}$$

throughout the contact region; hence the near-surface values are good approximations in themselves and no extrapolation is required. For the adhesive condition, the presence of boundary shears implies that (1.4) does not hold, so we use standard linear extrapolation in lieu of anything obviously better.¶

At first glance, it might appear that a similar extrapolation procedure would be required for the stresses down the vertical edge of the discretized quarter-circle. Since this is a symmetry axis though, each node has its semicircular array of elements mirrored in effect by a set with corresponding values and no extrapolation is necessary, as is the situation everywhere else for the nodal stresses themselves. On the other hand, when these nodal stresses are used to estimate the position of the edge of the yield region, some interpolation is required, as it is with nodal strains when finding contours of constant strain. Again, standard linear interpolation is used.

Even using nodal values some numerical noise persists, the greatest amount occurring in the contact stresses. To rid the results of these extraneous wobbles, we smooth the normal contact stress by fitting it with

$$\frac{\sigma_z}{p} = \left[C_1\left(1 + C_2\left(\frac{r}{a}\right)^2\right)\sqrt{1 - \left(\frac{r}{a}\right)^2} + C_3\right]U\left(1 - \frac{r}{a}\right), \tag{1.5}$$

wherein $p = P/\pi a^2$ is the average contact pressure, $C_i (i = 1, 2, 3)$ are the constants to be adjusted, and U is the unit step function. The form of (1.5) owes its origin to the stress-free condition outside the contact region, to σ_z's elastic predecessor, to the fact that σ_z is an even function of r, and to simplicity. The determination of C_i in eqn (1.5) is carried out by first ensuring that the correct average value is recovered on integration, and thereafter fitting the data in a least squares sense. For the other stress components in the contact area it is not so clear what is a reasonable function to fit. Thus we elect to avoid the difficulty in large part by limiting full presentation to nodal values just below the upper boundary—removing the need to *extrapolate* to the surface renders the data far less sensitive to numerical noise. For these last results and all others, we merely use hand-drawn fits with a French curve to obtain smooth plots.

While these smooth curves possess the advantage of removing the distracting high-frequency oscilations present in the underlying data—an especially attractive feature when displaying a number of curves in a single figure to show trends, *etc.*—it is nonetheless important to preserve some idea of the extent to which the results presented are subject to numerical noise. With this in mind, we introduce the *standard deviation* s calculated in accordance with

$$s = \sqrt{\frac{1}{N}\Sigma(f_d - f_f)^2}, \tag{1.6}$$

¶ In comparison with using nodal forces, these procedures resulted in slightly better agreement with the known exact solution for the frictionless condition on the first elastic load step, and seemingly less noisy results for both conditions with increasing amounts of plastic flow.

where N is the total number of data points fitted and f_d, f_f are values of the field quantity of interest taken from the data and the corresponding point on the fitted curve respectively. The standard deviation of (1.6) is calculated for each quantity in the figures that follow and the s so found tabulated in the Appendix. From these values, the reliability of the results given may be inferred, even if only in an informal fashion. Summarizing the standard deviations of the Appendix in this way, we estimate that, away from the surface, the results really do not suffer much from numerics, while near the surface they are probably accurate enough for meaningful engineering interpretations, but could nonetheless certainly be improved by a superior analysis in the future. In the meantime, we look to review the outcome of applying the foregoing elementary data reduction techniques.

2. RESULTS AND DISCUSSION

In this section, we start by comparing the results determined from our analysis with Tabor's experimental correlations for work-hardening materials, then use the findings from this appraisal to suggest a sensible way to present the overall indentation response in a plot showing indentation pressure versus extent. Next we consider the surface and interior stress distributions induced during loading up and on unloading. Finally, we view the accompanying deformation via curves depicting increasing yield regions and contours of constant strain at different load levels, and by means of the surface displacement profiles attending various loads, including corresponding recovery on unloading.

Preliminary to comparing the present analysis with *Tabor's experimental correlations*, we briefly review the basis of the latter's development, drawing on Tabor's classic monograph[5]. In [5, Ch. IV], Tabor first considers materials which have been highly worked and as a result have stress-strain curves which are nearly *perfectly plastic* post-yield—the stress-strain response that slip-line theory is most applicable to. By performing a series of experiments, Tabor establishes that, above a certain threshold level of indentation which defines the so-called *fully plastic* regime, the average pressure is given by

$$p \simeq 2.8\sigma_y, \tag{2.1}$$

nearly *independently* of further indentation. Moreover, this relationship is shown to hold for a variety of metals in [5]; indeed, while the constant in (2.1) is the average of the values reported in [5, pp. 51, 73] for a tellurium-lead alloy, aluminum, copper, and mild steel, the individual averages for these materials themselves only vary from 2.7 to 2.9. Give such wide applicability, (2.1) is distinctly helpful in practice, since it enables the average pressure p, which equals the *Meyer hardness* by definition, to be interpreted in terms of the more generally useful quantity, the *uniaxial yield stress* σ_y.

Motivated by a desire to preserve the relationship (2.1), or at least one like it, for *work-hardening* materials in the fully plastic regime, Tabor next seeks a *representative uniaxial yield stress* or *flow stress*, σ_f, to this effect in [5, Ch. V]. Of course, for materials which strain harden, not only does the yield stress increase with increased indentation, but it also varies spatially throughout the yield region even with the extent of indentation held fixed. Accordingly, it is not obvious how to select a single representative value for a given load level. To overcome this difficulty, Tabor examines a series of microhardness tests, made with a Vickers pyramidal indenter, on the surface of a large spherical indentation, then uses an earlier calibration to convert these microhardness measurements into yield stresses, thereby obtaining some information on yield stress variation. Tabor thus finds that, if the yield stress at the edge of the contact region is selected as being representative,

$$\sigma_f \simeq \frac{p}{2.8}, \tag{2.2}$$

throughout the fully plastic regime, *i.e.*, the counterpart of (2.1) is recovered. In addition, by appreciating the fact that geometric similarity insists that the *associated representative uniaxial strain* or *flow strain*, ϵ_f, must be a function of a/R alone, Tabor is able to observe that

$$\epsilon_f \simeq 20\,\frac{a}{R}\,, \tag{2.3}$$

wherein ϵ_f is in percent strain. Together, therefore, eqns (2.2), (2.3) enable one to back out, approximately at least, the post-yield stress-strain curve or flow curve for a material from hardness measurements; hence Tabor's correlations allow relatively simple tests to be used to estimate one of the most important of material characterizations in engineering.

All of the foregoing is founded on *experimentation*; our intent here now is to examine these findings *theoretically* for the work-hardening material we have analyzed. To this end, we simulate Tabor's approach with our finite element grid as described below. We first pick the interior node outside the contact region, yet nearest to the last node in contact, which is enclosed by the maximum number of elements any node is in this vicinity, namely 7 (Fig. 3(a)); in this way we try to provide data relatively free from numerical aberration and to approximate the position of the key microhardness test at the edge of the contact region. The precise location of this node changes with respect to the actual physical geometry because of variations in the local grid arrangement experienced as the contact region expands, but nonetheless it remains very close to $a/10$ outside the contact region and below the surface. For this node, we average octahedral strain values then convert them to uniaxial values to serve as our estimate of the flow strain ϵ_f for comparison with that of (2.3) (Fig. 3(b)). Lastly, we use the stress-strain curve (Fig. 2) to determine the flow stress σ_f associated with our finite element ϵ_f, divide this σ_f into the average pressure for a given indentation, and compare the ratio with that of (2.2) (Fig. 3(c)).

For the *strain correlation*, the agreement between the frictionless FEM results and those of Tabor's experiments is remarkable in view of the high strain gradients present, these last probably making major contributions to the scatter evident in the experimental points shown in Fig. 3(b). To substantiate this claim further, if the data given in Tabor[5, p. 73], up to and including values for $a/R = 0.7$, are averaged, the slope is found to be 20.7, whereas the slope of the FEM line in Fig. 3(b) for the frictionless condition is 20.9 (*cf.* 20 of (2.3)). In contrast, the FEM adhesive results are only in fair agreement with the experimental, the slope of the associated line in Fig. 3(b) being 16.1. This poorer agreement indicates, perhaps, that the physics of the situation is better captured by the frictionless condition, though possibly it is also caused to some degree by the greater numerical noise the adhesive condition provokes. For the *stress*

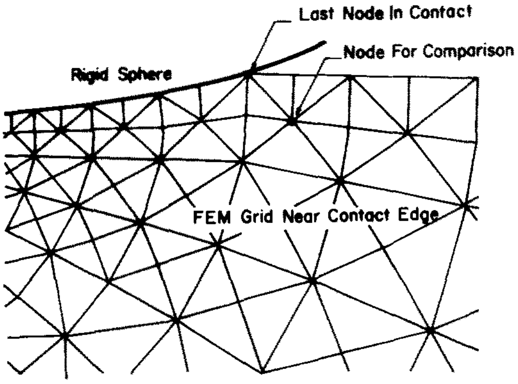

Fig. 3(a). Location of the node for comparison with Tabor's experiments.

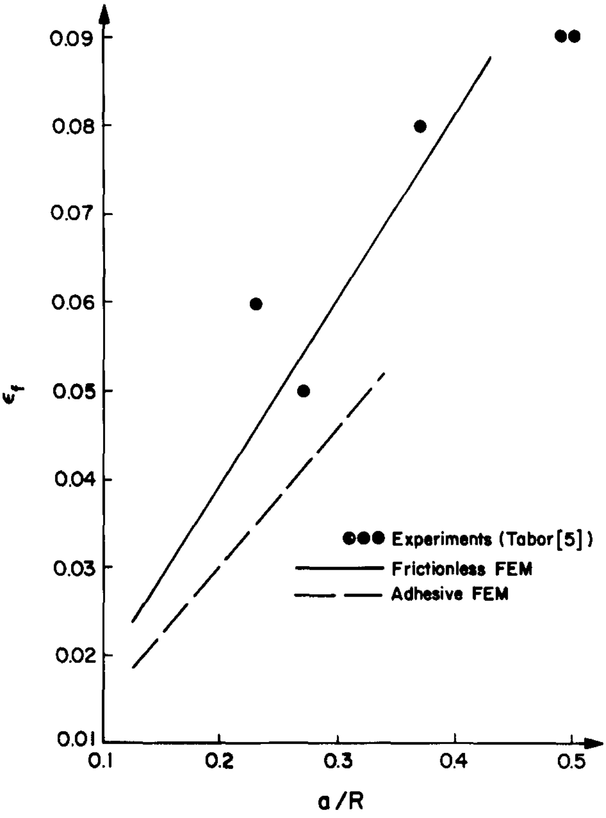

Fig. 3(b). Comparison with experimental strain correlation.

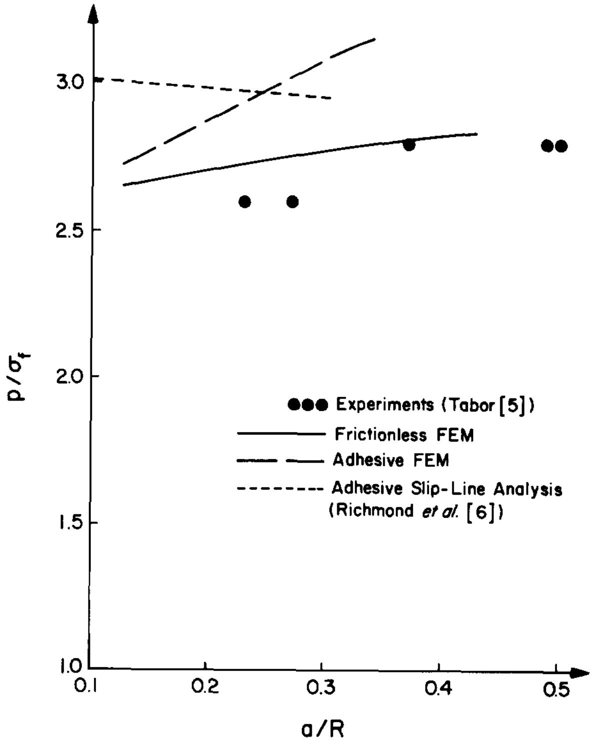

Fig. 3(c). Comparison with experimental stress correlation.

correlation, the agreement between the frictionless FEM results for p/σ_f and all the experimental points from Tabor[5, p. 73] that could be included in Fig. 3(c) is also good, both being within 8% of the 2.8 of (2.2) and showing slight increases with increasing indentation. The adhesive FEM is on average 5% higher in its p/σ_f value and once more does not fit the physical evidence as well as the frictionless. For this fully plastic response, too, there are available estimates from *slip-line theory*. The one we consider here is the slip-line analysis of an *adhesive* spherical indenter furnished by Richmond, Morrison, and Devenpeck[6], who note in passing that the slip-line treatment by Ishlinsky[7] of a perfectly *smooth* spherical indentor is in error; for comparison, we present their results as well in Fig. 3(c). These slip-line values of p/σ_f are typically higher than the FEM and not in as good agreement with the experimental values as the FEM are. In addition, they show a decrease with increasing a/R in contradiction to generally observed physical trends. Even so, they represent fair accord which could yet be improved with a correct slip-line analysis of the frictionless condition: the extent of this improvement can be estimated from values of p/σ_f for flat circular punches which are adhesive and frictionless, the pertinent analyses being in Eason and Shield[8] and Shield[9], respectively, and show a decrease in p/σ_f of 6% with the removal of all friction. Thus, in both types of analysis the effects of friction on p/σ_f are not great, as one would expect physically, since the predominant plastic flow is perpendicularly away from the indenting surface rather than parallel to it.

In all, the theoretical confirmation of Tabor's empirical correlations is quite reassuring and strongly suggests that, when evaluating the variation in the Meyer hardness over the entire region, the appropriate quantity to nondimensionalize it with is the *flow stress*: in this way, the response of all materials in the fully plastic regime should approach a common value of about 2.8. In attempting to preserve this material independence for other indentation extents so as to provide something akin to a *universal Meyer hardness curve*, we next turn to the initial elastic response to aid in selecting a suitable dimensionless measure of indentation extent.

Elastically, the average pressure or Meyer hardness is given by, from Hertz's classical solution[10],

$$p = \frac{4}{3\pi}\frac{E}{1-\nu^2}\frac{a}{R}. \tag{2.4}$$

To nondimensionalize, we divide by the flow stress, with the proviso that it never be less that the yield stress, *viz.*, we divide by

$$\sigma_f = \begin{cases} \sigma(\epsilon_f) \text{ if } \sigma(\epsilon_f) \geq \sigma_y, \\ \sigma_y \text{ otherwise,} \end{cases} \tag{2.5}$$

where $\sigma(\epsilon)$ is the stress from the uniaxial curve and ϵ_f is the flow strain of (2.3). Then (2.4), (2.5) offer the following quantity, which we denote by γ, as a measure of *indentation extent* for all materials in the elastic regime,

$$\gamma = \frac{E}{\sigma_f(1-\nu^2)}\frac{a}{R}. \tag{2.6}$$

Observe that an alternative and completely equivalent measure in the elastic regime is γ', where

$$\gamma' = \frac{E}{\sigma_y(1-\nu^2)}\frac{a}{R}, \tag{2.7}$$

by virtue of the fact that there is no yielding in this initial range so that σ_f remains at its initial value σ_y. To extend either of these measures into the elasto-plastic regime and on up into the fully plastic, we start by modifying Poisson's ratio to reflect the fact that we have assumed plastic flow to be incompressible. We do this by expanding the role of Tabor's representative strain ϵ_f, and taking, as a *representative Poisson's ratio*, ν_r, the average of the plastic value ($\frac{1}{2}$) and the elastic (ν), weighted by the excess of ϵ_f over the yield strain ϵ_y. This leads to

$$\nu_r = \begin{cases} \dfrac{1}{2}\left[1 - \dfrac{\epsilon_y}{\epsilon_f}(1 - 2\nu)\right] & \text{if } \epsilon_f \geq \epsilon_y, \\ \\ \nu \text{ otherwise.} \end{cases} \tag{2.8}$$

For convenience, we define a corresponding *representative modulus* E_r by

$$E_r = \frac{E}{1 - \nu_r^2} \, . \tag{2.9}$$

Now, as σ_f and σ_y no longer remain equal throughout the elasto-plastic regime, we consider which of the two candidates in (2.6), (2.7) better extends into this regime with a view to coalescing all material responses into a single curve as much as possible. To make the decision, we invoke the following simple approximate argument. Imagine a material such that it yields when its unaxial stress reaches σ_y, but thereafter flows incompressibly whilst work-hardening with an exponent of one, the ultimate in strain-hardening materials in effect. Then, to a first approximation we can expect its behavior to be characterized by

$$\frac{p}{\sigma_f} = \frac{4}{3\pi}\frac{\sigma_y}{\sigma_f}\frac{aE_r}{R\sigma_y} \, . \tag{2.10}$$

Moreover, curiously enough, as $a/R \rightarrow \infty$ in (2.10) we find, via (2.3), (2.5), (2.8), and (2.9), $p/\sigma_f \rightarrow 20/3\pi(1 - 0.5^2) = 2.83$, so that such a *quasi-elasto-plastic material* comes very close to our common fully plastic asymptote of 2.8. For this ultimate of materials, the choice of the first ratio, (2.6) with $E/(1 - \nu^2)$ therein replaced by E_r, as a measure of indentation extent, means that our hardness curve, or plot of p/σ_f versus γ, ends abruptly as a/R increases, because γ has an upper bound of $5/(1 - 0.5^2) = 6\frac{2}{3}$. On the other hand, the choice of the second ratio, (2.7) on introducing E_r, gives a measure that increases without limit. As this is also the case with either ratio for real materials with work-hardening exponents less than one, we fix our choice on the second. Thus our attempt to furnish a universal Meyer hardness curve features a graph of p/σ_f versus $aE_r/R\sigma_y$ (Fig. 4).†

The commentary on the curve in Fig. 4 is aided by being focused, in turn, on each of the three regimes comprising the entire deformation spectrum: the *elastic*, the *elasto-plastic*, and the *fully plastic*. The boundary between the first two can be determined from Huber's amplification[12] of Hertz's elastic solution[10]. To do this, we assemble the octahedral shear stress from the expressions in [12] and set it equal to the value for initial yielding. The outcome of the exercise is that, *at yield*,

$$\begin{aligned} \frac{p}{\sigma_y} &= \frac{4}{3\pi}\frac{aE}{R\sigma_y(1 - \nu^2)} \\ &= \min_{0 \leq z/a < \infty} \frac{2}{3}\Bigg/\left[(1 + \nu)\left(\frac{z}{a}\cot^{-1}\frac{z}{a} - 1\right) + \frac{3}{2}\left(1 + \left(\frac{z}{a}\right)^2\right)^{-1}\right], \end{aligned} \tag{2.11}$$

† The nondimensionalizing of the hardness curve arrived at here, while somewhat different in detail, owes its spirit to that first put forward by Johnson[11].

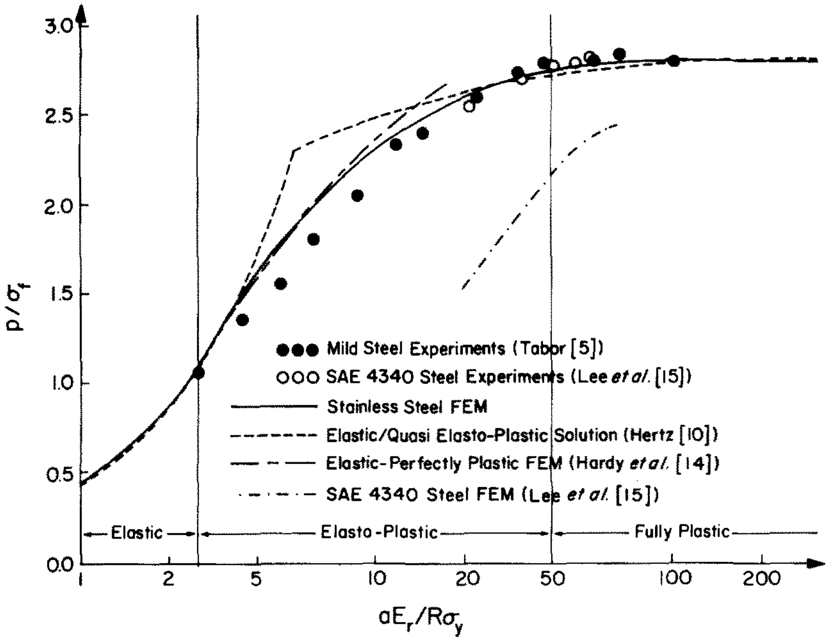

Fig. 4. Meyer hardness dependence on indentation extent.

which occurs at the point of first yielding, this being on the axis of symmetry at a depth given by‡

$$\frac{z}{a} = 0.382 + 0.332\nu. \tag{2.12}$$

Hence there is some dependence on the material being considered which enters through Poisson's ratio. The actual variations, though, are not great and all materials have values at yield within ±20% of those of the stainless steel treated here which are, from eqns (1.3), (2.11), (2.12),

$$\frac{p}{\sigma_f} = 1.1, \quad \frac{aE_r}{R\sigma_y} = 2.5. \tag{2.13}$$

The boundary between the elasto-plastic and fully plastic regimes heralds the onset of geometrically self-similar responses with p/σ_f remaining constant, at least to a good approximation. Its position is far less precisely determined, both in terms of its very definition and in practice with different materials. This last is true because, although we have basically set the level of p/σ_f at this boundary as being 2.8, the corresponding value of $aE_r/R\sigma_y$ seems to vary appreciably from one material to another. Here we find, for our stainless steel analysis, that the beginning of the plastic region occurs at

$$\frac{p}{\sigma_f} = 2.8, \quad \frac{aE_r}{R\sigma_y} \simeq 50. \tag{2.14}$$

The range of values of $aE_r/R\sigma_y$ evident in (2.13), (2.14) prompts the use of the log scale in Fig. 4.

For the elastic region, comparing the *FEM result for stainless steel* under the *frictionless* contact condition with *Hertz's solution*[10], which is also for perfectly smooth contact, we find that the finite element values display the usual overly stiff

---

‡ The two figure accuracy in yield point position represented by the simple approximate formula (2.12) leads to ample accuracy (five figures) in the actual values in (2.11) at yield.

response that minimizing potential energy produces, but are nonetheless in good agreement (Fig. 4). Both curves in this regime terminate at the same indentation extent ($aE_r/R\sigma_y$) with the finite element showing a 3% increase in hardness (p/σ_f) over the exact solution; this point is within 1% of the same indentation extent as the yield point for mild steel recorded in Tabor[5, p. 57], with the latter sharing the same hardness as the exact solution at the end of the elastic regime. Moving into the elasto-plastic regime, we see that the frictionless FEM values for stainless steel lie *below* those for the *quasi-elasto-plastic* material of (2.10), which has a strain-hardening exponent n of one, yet *above the empirical results* of Tabor[5, p. 57] for highly-worked mild steel, which has an n close to zero. Thus, in part, the divergence of our finite element results from the physical evidence in this region can be attributed to the greater strain-hardening of the stainless steel ($0.15 \leq n \leq 0.45$). However, a portion of this gap is almost certainly due to a continuation of, or even an increase in, the unduly stiff FEM response that began in the elastic regime. On considering experimental values for other materials in the elasto-plastic regime using the phenomenological summary of a number of different investigators assembled by Francis[13], we find, once our results are converted to the nondimensionalization employed in [13], that our FEM curve lies within the experimental scatter but near the upper values of p/σ_f. Lastly, in the *fully plastic* regime, if the flow stress of (2.5) is used to normalize hardness rather than its FEM counterpart as in Fig. 3(c), our finite element results level out to all intensive purposes at a constant value of *dimensionless hardness of 2.8,* in good agreement with the experimental results of Tabor[5] in this regime.§ Hence it would appear that the present frictionless FEM treatment is good enough to be physically meaningful, but could probably benefit from the reduction in stiffness that would attend an analysis with a still more refined grid than in use here.

For our hardness curve, we again find that the *effects of friction* are not that significant, our adhesive FEM analysis shadowing the frictionless curve of Fig. 4 while remaining of the order of 3% above it, and culminating in a fully plastic dimensionless hardness of 2.9. Again too, since the frictionless FEM response is, if anything, on the high side, these adhesive results are less attractive in their physical agreement.

Also depicted in Fig. 4 are the results of *other analyses,* these being confined to finite element investigations based upon the incremental theory of elasto-plasticity and excluding slip-line analyses, since the latter cannot track the deformation through the elasto-plastic regime. In the first of the other FEM analyses, Hardy, Baronet, and Tordion[14] study the indentation of an elastic-perfectly plastic half-space by a frictionless rigid sphere up to an intermediate level of indentation in the elasto-plastic regime (maximum $aE_r/R\sigma_y \simeq 20$). The FEM grid used in [14] is of comparable refinement to that here and initially, near the yield point, similar results are obtained. Subsequently, though, the use of the rescaling technique of [2] in our analysis preserves resolution, while that in [14] decreases. As a result, Hardy *et al.*[14] are at variance with the physical evidence significantly more than the present analysis is—in making this comparison we are bearing in mind that the material in [14] has a hardness exponent of zero, so that [14] should, therefore, be even closer to Tabor's values in Fig. 4 than our analysis, whereas in fact it ultimately exceeds the limiting curve for an exponent of one. In the second of the other FEM analyses, Lee, Masaki, and Kobayashi[15] treat the indentation of a large block of SAE 4340 steel by a frictionless rigid sphere up into early in the fully plastic regime (maximum $aE_r/R\sigma_y \simeq 65$). The FEM grid used in [15] is not given, but, to judge from the relative slope of the response plotted in Fig. 4 at the same extent of indentation, is stiffer and therefore coarser than that here. Too, the contact region at the outset in [15] consists of ony a single node—accordingly, the block in [15] starts with the numerical analogue of a singular point loading. This extreme of loading renders the indented materially so initially compliant that it never fully recovers, thus accounting for the very low dimensionless hardness displayed in Fig.

---

§ For further evidence of agreement in the fully plastic regime, see [2, Fig. 6] which is an enlarged plot of the fully plastic response in effect and compares the FEM results with experiments on the actual stainless steel analyzed.

Table 1. Indentations selected for frictionless contact

Indentation extent		Flow stress	Load levels	
a/R	aE_r/σ_y	σ_f/σ_y	p/σ_f	P/P_y
0.0127	11	1.04	2.4	45
0.0587	61	1.24	2.8	1,300
0.3164	334	1.66	2.8	52,000

4. In marked contrast to their analysis, Lee *et al.*'s rather careful experiments (included in Fig. 4) lie in close proximity to our hardness curve and Tabor's experimental values.

Turning to a review of the stresses accompanying indentation, the success of the flow stress of (2.5) in condensing the responses for different materials into a narrow band about the same curve in Fig. 4 suggests its continued use to nondimensionalize these results so that they, too, may become approximately material independent. Figure 4 also indicates appropriate load levels to gauge the different types of response; accordingly, we limit the graphical presentation of results to three, the minimum set judged sufficient to show trends with increasing indentation, and merely comment on intervening loads.¶ The three load levels/indentation extents chosen from our frictionless FEM treatment reflect behavior in the elasto-plastic regime, early in the fully plastic regime and well into the fully plastic regime. Details of these indentations in the frictionless instance are given in Table 1, wherein P_y is the load required to just induce yielding in the half-space, evaluated via (1.3), (2.11); in what follows, we distinguish corresponding curves by their values of a/R, taken from the first column of Table 1. We confine the bulk of the results examined to be those associated with the frictionless condition rather than the adhesive, as the former would seem to agree better with the physical evidence and to be less subject to numerics. We do, though, furnish some adhesive results at similar indentations when numerical noise effects are judged to be of no consequence.

We begin our examination with the *contact stresses* since some companion experimental results are available from which we can infer physical applicability. Figure 5 displays the frictionless *normal contact stress* σ_z, nondimensionalized by σ_f, as a function of position r/a for the three indentations of Table 1, together with the results for on the point of yield, namely, from Hertz[10],

$$\frac{\sigma_z}{\sigma_f} = \frac{-3p}{2\sigma_f}\sqrt{1-\left(\frac{r}{a}\right)^2}, \tag{2.15}$$

with p/σ_f as in (2.13). Though the transition from elastic to elasto-plastic and fully plastic is somewhat obscured because of the scales employed to enable presentation in a single figure, it is nonetheless clear in Fig. 5 that the distribution approaches a virtually *uniform* one with almost no change with indentation in the fully plastic regime. Further, 75% of the change in the fully plastic results occurs as the indentation ($aE_r/R\sigma_y$) goes from 11 to 134, with the remainder taking place as it progresses to 334, so that the later part of the response is very close to a steady-state or self-similiar one. These distributions remain basically unaltered under the adhesive condition, at least so far as the present FEM can detect, but there are indications of an increase in average σ_z/σ_f of the order of 3% for all three of the different indentations.

In evaluating our FEM determination of the contact pressure, we begin by noting that, although not included in Fig. 5, agreement with the elastic solution is good (see

---

¶ In this connection, we remark that there are some significant engineering implications to be drawn from results earlier in the elasto-plastic regime than those given here. Unfortunately, we are unable to do this, since we lacked the foresight to maintain a sufficiently complete record of the initial plastic flow calculations. However, these results are the easiest to compute and, because of the small number of load steps entailed, could be recalculated to better effect with an even more refined grid than that of [2] or [14], an exercise which we believe would make a worthwhile contribution.

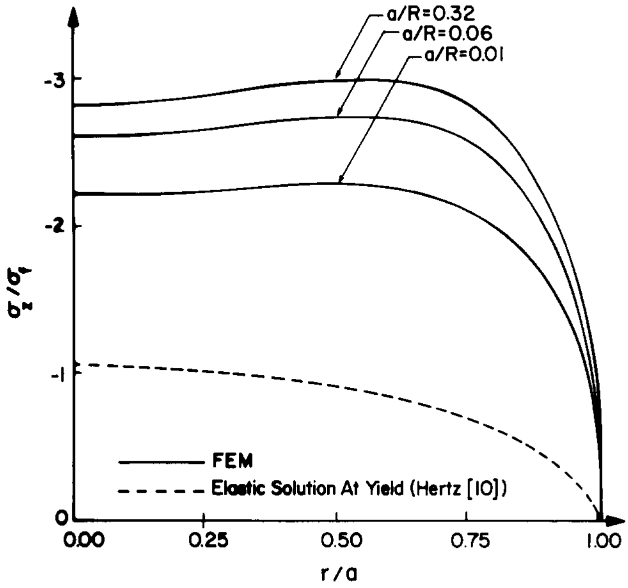

Fig. 5. Frictionless contact pressure distributions.

[2]). For the elasto-plastic response, the flattening of the contact pressure shown in Fig. 5 is also found in Hardy *et al.*'s analysis[14]. In the fully plastic regime, the nearly uniform contact pressures agree well with the experimental study conducted by Johnson[16] which finds the pressure to be completely constant, at least to within the resolution possible in [16]. In this connection, too, if we continue to interpret the elastic solution as a quasi-elasto-plastic response, but modify it by replacing the parabolic approximation to the indenter profile with its more appropriate exact counterpart, we find in the closed form solution to the *plain strain* analogue in Cinar and Sinclair[17], that the pressure distribution approaches a uniform one as $a \to R (a < R)$. In all, then, the consensus has it that there is a nearly *constant contact pressure* in the *fully plastic* regime.

In assessing the ability of *slip-line theory* to predict the contact pressure distribution we are impeded by an absence of such information in Richmond *et al.*[6], and by lack of a means to accurately estimate the effects of the errors in the analysis in Ishlinsky[7] on the contact stress distribution given therein. Nonetheless, slip line theory would seem to give a significantly nonuniform distribution with a maximum at the center. More precisely, the questionable results of [7] have a maximum pressure $p_{\max}$ at $r/a = 0$ and a minimum $p_{\min}$ at the outer edge, $r/a = 1$, with $p_{\max}/p_{\min} = 1.64$. Furthermore, some of the uncertainty that this is a valid result even within the limitations of slip-line theory is removed by Shield's analysis[9] for a smooth *flat* circular indenter which has maximum and minimum contact pressures at the same locations with $p_{\max}/p_{\min} = 1.41$. As this flat punch problem has a far lower value of the ratio of the pressures at these locations in its elastic antecedent than the spherical indentation problem (0 *cf.* ∞ in fact), it would seem that $p_{\max}/p_{\min}$ in the slip-line treatment of the latter should be at least 1.41. The slip-line result is therefore in direct contradiction to that here, which has $p_{\max}$ at $r/a \simeq 0.6$, and if we avoid the ambiguity of defining a minimum near the outer edge where the boundary conditions insist that p approach zero and look only inside this station, a minimum at the center, with $p_{\max}/p_{\min} = 1.07$. Empirically, of course, Johnson[16] has $p_{\max}/p_{\min} = 1.00$. Hence slip-line theory appears to fail to predict the contact stress *distribution* fairly comprehensively. This failure may be due, in part, to an absence of work hardening in slip-line theory, though it would seem to persist in materials that do not harden greatly (as in Johnson[16]). More probably, the failure is due to the fact that slip-line theory cannot allow for the effects of elastic deformation, which can be significant even in the fully plastic regime because the albeit relatively small elastic strains are felt over a relatively large volume compared to the plastic, so that the elastic "give" is not negligible and tends to lower the contact pressure required for large indentation, especially in the middle. In sum, slip-line theory looks to be incapable of furnishing good estimates of the contact pressure distribution for the problem at hand and probably for others like it.

Turning to the *other contact stress components*, we find that, essentially, our FEM treatment fails to reliably detect any differences between the frictionless σ_r and σ_θ distributions and gives, in the elasto-plastic regime,

$$\frac{\sigma_r}{\sigma_z} \simeq \frac{\sigma_\theta}{\sigma_z} \simeq 0.83 \left(\frac{a}{R} = 0.01\right), \qquad (2.16)$$

and in the fully plastic regime

$$\frac{\sigma_r}{\sigma_z} \simeq \frac{\sigma_\theta}{\sigma_z} \simeq 0.68 \left(\frac{a}{R} = 0.06, 0.32\right). \qquad (2.17)$$

The corresponding adhesive results cannot be distinguished from those of (2.16), (2.17), while the shear stress in the contact region under the adhesive condition is relatively small. These normal contact stresses compare quite well with those for frictionless elastic indentation which have $\sigma_r/\sigma_z \simeq \sigma_\theta/\sigma_z \simeq 0.8$ throughout most of the contact region, and with Johnson's experimental determination[16] in the fully plastic regime which has $\sigma_r/\sigma_z \simeq \sigma_\theta/\sigma_z \simeq 0.6$.† More detailed information on the actual distributions than that contained in (2.16), (2.17) is not provided because of numerical noise; instead, we next look at near-surface but interior stress distributions where the results are free from the numerics provoked by extrapolation to the surface.

Near-surface interior stresses are displayed in Fig. 6(a), which shows the frictionless radial and hoop stress components σ_r, σ_θ, normalized by the flow stress σ_f, along a ray emanating from the origin at an angle of $\pi/32$ below the surface, as functions of ρ/a where $\rho = \sqrt{(r^2 + z^2)}$ is the distance from the origin. Several comments are in order. In this neighborhood, these stress components are approximately principal so that, under the Haar-von Karman assumption used in slip-line theory, they should be nearly equal. For $\rho < a$ the two stress components are very nearly equal, in close accord, therefore, with this assumption. However, as ρ exceeds a and the boundary of the yield region is approached ($\rho \simeq 2a$), this assumption does not hold, σ_r remaining significantly compressive while σ_θ is nearly zero and if anything slightly tensile—while little faith should be put in our FEM treatment's ability to determine these tensile stresses precisely because of their relatively low magnitudes, it is worth noting that every FEM output for indentation extents greater than or equal to $a/R = 0.06$ had some tensile hoop stress outside the contact region. For all values of ρ/a, the results for the two upper indentations are quite similar, indicating an almost steady-state fully plastic response for these components as well.

Stresses deeper within the interior are given in Fig. 6(b), which presents the σ_z, σ_r stress components, nondimensionalized by the flow stress, along a ray inclined at $\pi/4$ to the upper surface. Here σ_z, σ_r are compressive throughout, with σ_z larger in magnitude than σ_r until around a station directly below the edge of the contact region; thereafter, $|\sigma_r|$ tends to exceed $|\sigma_z|$ as both decay to zero. Though not shown in Fig. 6(b), the other normal stress component, σ_θ, remains close to σ_r until out from under the contact region, then decays somewhat more rapidly much in the same way as in Fig. 6(a). Again, too, the fully plastic results are close to a steady state.

Stresses down the axis of symmetry are furnished in Figs. 6(c) and 6(d). For this location, numerical noise is apparently almost nonexistent even for the adhesive contact, so that direct comparisons between the frictionless and adhesive stresses can be made, first in Fig. 6(c) for σ_z/σ_f, second in Fig. 6(d) for σ_r/σ_f, which equals σ_θ/σ_f along

† The elastic comparison is not viable over the entire contact region, as these ratios go ∞ at the contact edge; nonetheless the result stated holds over the inner 80%.

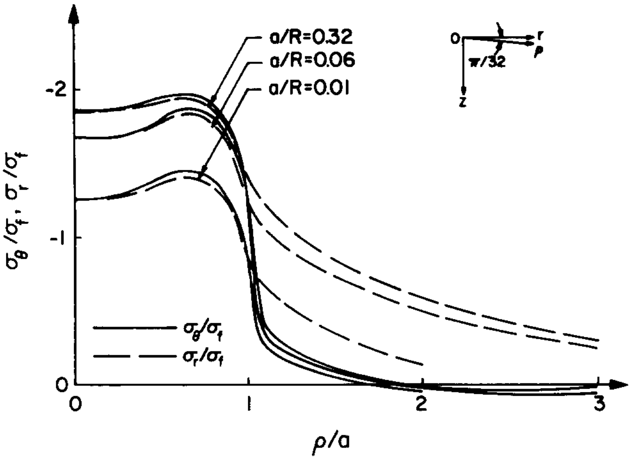

Fig. 6(a). Interior stress distributions: near surface.

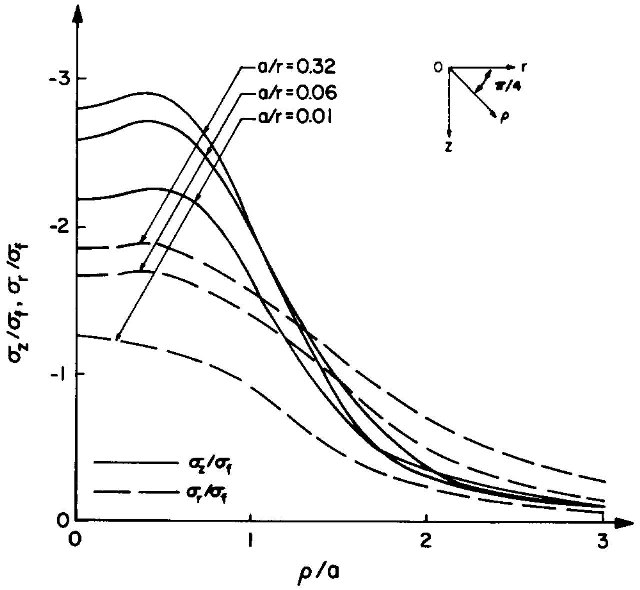

Fig. 6(b). Interior stress distributions: along 45° ray.

this axis. The frictionless results for the axial stress σ_z show zero slope at the upper surface as required in (1.4), and are larger in magnitude than the adhesive σ_z; at the near surface maximum, though, the adhesive $|\sigma_z|$ are slightly higher; below the peak magnitudes both results display a similar rate of decay and there is little dependence on the choice of contact condition as expected. This pattern is repeated for the radial stress σ_r (alternatively, the hoop stress σ_θ), although here the slopes of the frictionless values are not quite zero at the surface. Both figures continue the demonstration of results which are nearly independent of indentation extent in the fully plastic regime, with these fully plastic results being in fair agreement with the interior axial stresses inferred from surface measurements in Johnson[16].

Turning to the *residual stress distributions*, we begin by examining the possibility of *reverse plastic flow on unloading*. We do this by adapting Johnson's argument[18] to reflect the fact that our contact pressure is constant throughout the contact region to all intents and purposes. Thus we consider the effect of elastic unloading by superimposing the response of an elastic half-space to a *uniform tension* acting over a circular patch on its surface. From Love's solution[19] for this elasticity problem, particularly from the discussion of [19] in Timoshenko and Goodier[20, pp. 406, 407], we find that the maximum difference in the principal stresses on the axis of symmetry occurs at a

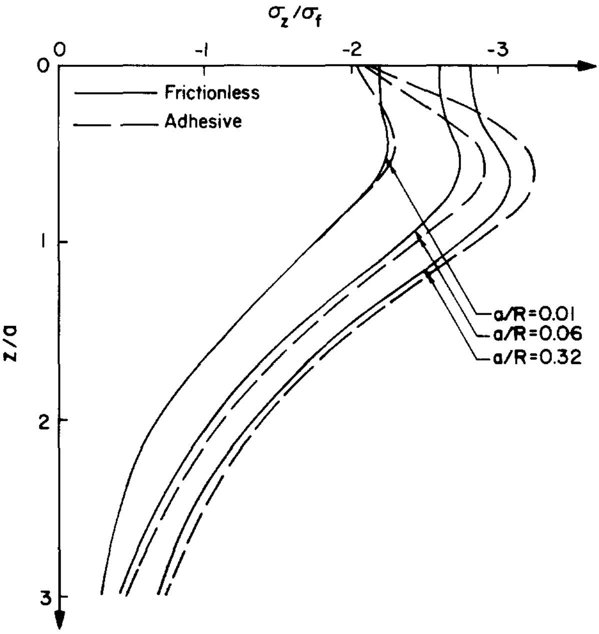

Fig. 6(c). Interior stress distributions: axial stress on axis of symmetry.

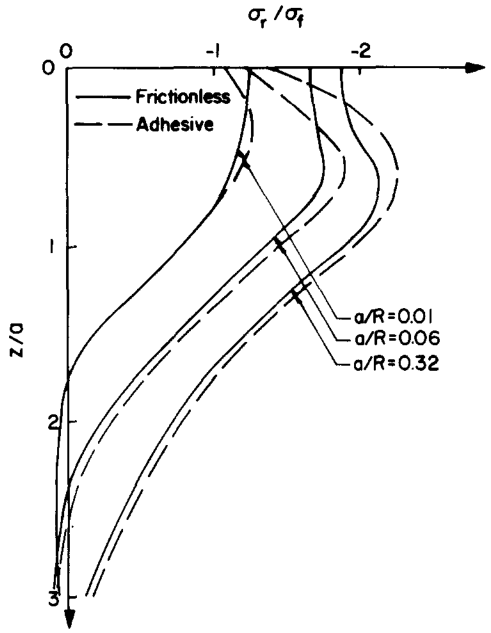

Fig. 6(d). Interior stress distributions: radial stress on axis of symmetry.

depth $z/a = 0.63$ for our material ($\nu = 0.28$), and is given by $\sigma_z - \sigma_r = 0.675p$. Hence, combining this with corresponding differences on loading up (Figs. 6(c), 6(d) at $z/a = 0.63$), taking due account of sign, we have: for elastic unloading from the elasto-plastic regime,

$$\sigma_z - \sigma_r = 0.56\sigma_f = 0.58\sigma_y \left(\frac{a}{R} = 0.01\right), \tag{2.18}$$

while on elastically unloading from the fully plastic regime,

$$\begin{aligned} \sigma_z - \sigma_r &= 0.89\sigma_f = 1.10\sigma_y \left(\frac{a}{R} = 0.06\right), \\ \sigma_z - \sigma_r &= 0.93\sigma_f = 1.54\sigma_y \left(\frac{a}{R} = 0.32\right). \end{aligned} \tag{2.19}$$

What (2.18), (2.19) in essence have is that *if* we assume that the material *work-hardens isotropically* there is probably no reverse yielding, since $\sigma_z - \sigma_r$ is uniformly less than σ_f; on the other hand, if the yield point in tension remains unaltered by working the material in compression, or, as in the Bauschinger effect, even drops below its initial value, reverse yielding can be expected on unloading from the fully plastic regime, as then $\sigma_z - \sigma_r$ exceeds σ_y. Consequently, it is basically the simplifying assumption of isotropic work-hardening made in our analysis and incorporated into the accompanying FEM code that leads us to ignore reverse plastic flow.

An additional impediment to employing simple elastic superposition to model unloading stems from the nature of the radial and hoop stress components in the elastic solution at the surface outside the contact region. Here elastic unloading *adds* to the compressive radial component and *increases* the tension in the circumferential direction. As a result, further *plastic flow* must take place. However, we expect the effects of such continued flow, together with those attributable to reverse flow, to be small, at least for a single loading to judge from the reversible responses reported in Tabor[5, pp. 84, 85] for several repeated loading and unloadings. We therefore use elastic superposition to furnish estimates of the residual stresses here.

The actual forms for elastic superposition can be constructed from expressions given in Love[19] and are:

$$\begin{aligned} \sigma_z &= \frac{p}{2}\left[1 - \frac{r^2}{\delta^2}\,\zeta E(k')(\rho^2 - a^2) + \operatorname{sgn}(a - r)\left(1 - \Lambda_0\left(k', \frac{z}{\delta}\right)\right)\right], \\ \sigma_r &= \frac{\mathrm{p}}{4}\left[\xi + \zeta\left(K(k')(\eta^2 - 4\nu r^2) - E(k')\left(2(1 - \nu)\delta'^2\right.\right.\right. \\ &\quad \left.\left. + \frac{(k^2 + 1)}{2k^2}(a^2 + z^2 - r^2)\right)\right) + \operatorname{sgn}(a - r)\xi'(1 - \Lambda_0\left(k', \frac{z}{\delta}\right)\Big)\Big], \\ \sigma_\theta &= \frac{p}{4}\left[\xi' - \zeta\left(K(k')(\eta^2 + 4r^2) - E(k')(3 - 2\nu)\delta'^2\right)\right. \\ &\quad \left. + \operatorname{sgn}(a - r)\,\xi\left(1 - \Lambda_0\left(k', \frac{z}{\delta}\right)\right)\right], \end{aligned} \tag{2.20}$$

where $\operatorname{sgn}(a - r)$ is the signum function, $\Lambda_0(k, \Psi)$ Heuman's lambda function, and $K(k)$, $E(k)$ are complete elliptical integrals of the first, second kinds respectively, these being defined by

$$\begin{aligned} \operatorname{sgn}(a - r) &= (a - r)/|a - r| \; (a \neq r), \\ \Lambda_0(k, \Psi) &= \frac{2}{\pi}[K(k')E(k, \Psi) - (K(k') - E(k'))F(k, \Psi)], \\ K(k) &= F(k, 1), E(k) = E(k, 1), \end{aligned} \tag{2.21}$$

where $F(k, \Psi)$, $E(k, \Psi)$ are incomplete elliptical integrals of the first, second kinds respectively, defined in accordance with

$$\begin{Bmatrix} F(k, \Psi) \\ E(k, \Psi) \end{Bmatrix} = \int_0^{\Psi} (1 - k^2\Psi)^{\{\mp\}1/2} \frac{\mathrm{d}\Psi}{\sqrt{1 - \Psi^2}}. \tag{2.22}$$

Further, in (2.20),

$$k = \frac{\delta}{\delta'},\ k' = \surd(1 - k^2),\ \zeta = \frac{2z}{\pi\delta' r^2},$$

$$\begin{Bmatrix}\delta\\ \delta'\end{Bmatrix} = \sqrt{\left[\left(r\begin{Bmatrix}-\\ +\end{Bmatrix}a\right)^2 + z^2\right]},\qquad \begin{Bmatrix}\xi\\ \xi'\end{Bmatrix} = 1 + 2\nu\begin{Bmatrix}-\\ +\end{Bmatrix}(1 - 2\nu)\frac{a^2}{r^2},\tag{2.23}$$

$$\eta^2 = 4(1 - \nu)a^2 + (3 - 2\nu)z^2,\qquad \rho^2 = r^2 + z^2.$$

The results of superimposing the stresses of (2.20)–(2.23), on the frictionless interior stresses under loading given in Figs. 6, are shown in Figs. 7.

The first of such figures, Fig. 7(a), displays *near-surface, residual, radial, and hoop stresses*. Both of these components approach a tensile limit of around 0.35 σ_f at the center of the contacted surface. This value is in fair agreement with that inferred from experiments by Johnson[16] of 0.45 σ_f (on converting the average yield stress in [16] to σ_f). Outside the contact region, the *hoop stress* σ_θ *increases* in its *tensile* magnitude on unloading, consistent with the observation of increased *radial cracking on load removal* (see *e.g.* Studman and Field[21]).

Figure 7(b) presents *residual stresses on an intervening ray* between that of Fig. 7(a) and *the axis of symmetry*, the latter having residual stresses as drawn in Fig. 7(c).

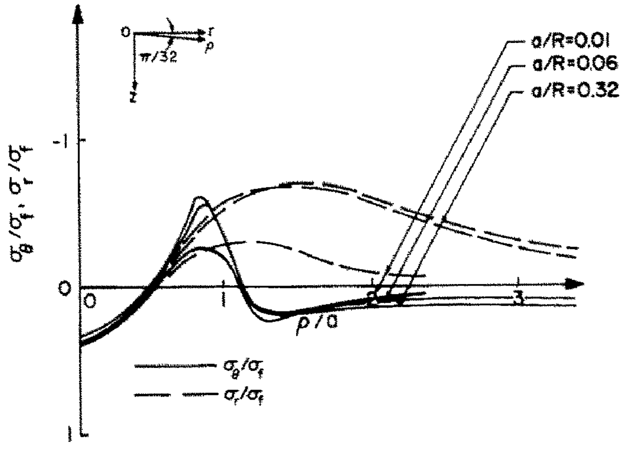

Fig. 7(a). Residual stress distributions: near surface.

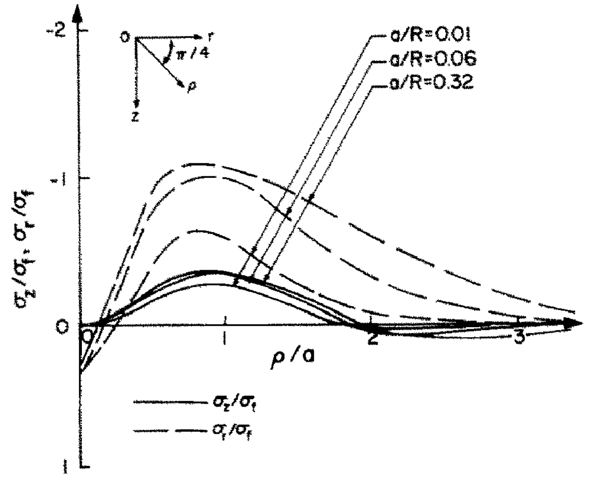

Fig. 7(b). Residual stress distributions: along 45° ray.

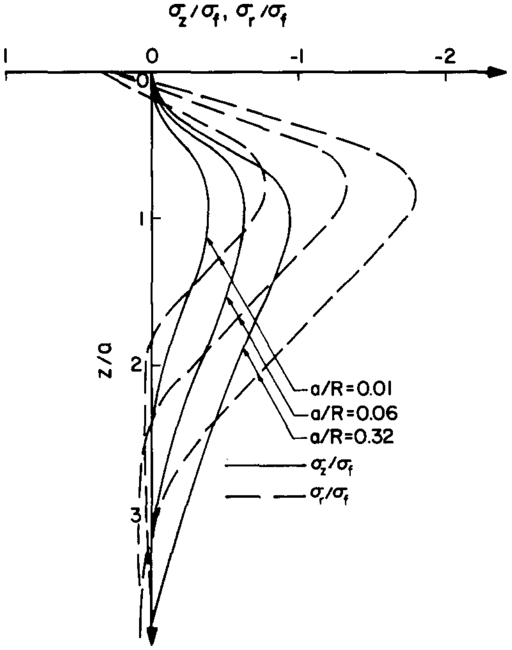

Fig. 7(c). Residual stress distributions: on axis of symmetry.

All three figures show that there is a shallow layer near the surface in which the radial (or hoop) stress is *tensile*; the depth of this layer in Fig. 7(c) reaches between 0.10a and 0.13a in the fully plastic regime (*cf.* 0.16a in Johnson[16]). Such fields may explain in part the general observation that fatigue and wear, which are predominantly driven by tensile stresses, occur most readily in the surface layers of materials rather than the subsurface (as discussed in, for example, Almen and Black[22]). Furthermore, the presence of tensile residual surface stresses raises questions concerning peening operations wherein the intent is to induce compressive residual stresses in the surface by repeated hammering or bombardment with hard shot. While the physics modeled here differs from that of such processes, most notably in treating only a single load application, the results in Figs. 7 do suggest tensile residual stresses at the surface as a possible outcome of peening at some stage. It is not clear from the present investi-

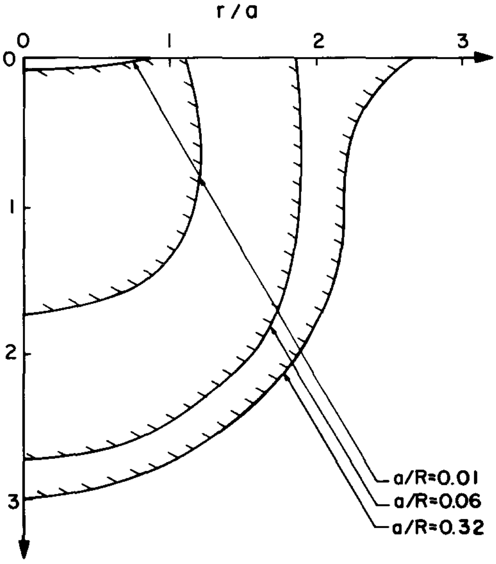

Fig. 8. Yield regions.

gation whether this tensile boundary layer is then counteracted by continued peening or quickly removed by wear in service to expose the sought-after surface with compressive residual stresses. Conceivably, though, a future and far more extensive study could identify and follow the mechanisms involved in peening.

Now turning to the *deformations* that attend the foregoing stresses, we start by examining the *regions of yielded material* under our selected loads for the frictionless contact condition (Fig. 8). In Fig. 8, the partial sectioning indicates the side of the elastic-plastic boundary on which the material is yielded, and the portion of the yield region boundary nearest the origin is only associated with the lowest load level ($a/R = 0.01$). This elastic enclave in the elasto-plastic regime can be anticipated from the distributions in the elastic solution (Huber[12]), and is also computed to exist in this regime in the finite element analysis of Hardy *et al.*[14]. The shapes of the yield regions in the fully plastic regime bear comparison with those found experimentally using etching (under the assumption of a simple compressive strain distribution) by Samuels and Mulhearn[23]. The radial and axial extremes of the strain regions with increasing levels of indentation taken from Fig. 8 and Samuels and Mulhearn[23] are: at yield,

$$\begin{aligned}
&\frac{r}{a} = 1.9, \qquad \frac{z}{a} = 2.8\left(\frac{a}{R} = 0.06, \text{ analytical}\right), \\
&\frac{r}{a} = 2.7, \qquad \frac{z}{a} = 2.7\left(\frac{a}{R} = 0.19, \text{ experimental}\right), \\
&\frac{r}{a} = 2.7, \qquad \frac{z}{z} = 3.0\left(\frac{a}{R} = 0.32, \text{ analytical}\right), \\
&\frac{r}{a} = 4.0, \qquad \frac{z}{a} = 4.4\left(\frac{a}{R} = 0.51, \text{ experimental}\right),
\end{aligned} \tag{2.24}$$

and at 1% strain,

$$\frac{r}{a} = 2.5, \qquad \frac{z}{a} = 2.5\left(\frac{a}{R} = 0.51, \text{ experimental}\right). \tag{2.25}$$

In addition to the reasonable quantitative agreement evident in (2.24), (2.25), the shape of the yield regions are qualitatively similar, both experimental and analytical determinations giving an approximate semi-ellipse with its major axis coinciding with the z-axis. A partial exception to this last is the near-surface turnover found in all finite element calculations for $a/R > 0.06$. There are insufficient data in this region to establish empirical support or disagreement with this analytical finding. At this point, then, it is not obvious whether such effects are attributable to systemic errors in the later finite element calculations or whether they are real. In any event, the yield regions continue the illustration of nearly steady-state response in the fully plastic regime.

Greater detail of the *strain distributions* attending loading in the fully plastic regime is available in Figs. 9, which display contours of constant octahedral strain (in %) for two frictionless contact conditions. By virtue of being a root mean square of sorts of the individual strain components, the octahedral strain tends to be free from numerics so that corresponding adhesive results are also provided in Figs. 10. The frictionless and adhesive contours display some differences near the contact surface and little away from it as expected. Both show *high strain gradients* near the edge of the contact region yet just below the surface, thus illustrating our earlier remark concerning scatter in Tabor's strain correlation (recall that it was this vicinity that Tabor selected as representative in effect). It is in this region, too, that the high strains contribute to the greatest strain reversals on repeated "impact" in the fatigue model for particulate erosion at sufficiently low speeds advanced in Follansbee, Sinclair, and Williams[24].

Right at the surface, the curves in Figs. 9 and 10 represent the corresponding displacement profiles to scale.

An enlarged view of the *displacement profiles* is provided in the non-cartesian plots of Fig. 11. Here on *loading up* we initially see indications of "sinking-in" ($a/R = 0.01$), then eventually in the fully plastic regime, evidence of "piling up". This sequence of responses is in accordance with the physical observation of Tabor[5, p. 15], that there is a propensity to shift from "sinking-in" to "piling-up" as a material becomes worked to a greater extent. Also shown in Fig. 11 are the *unloaded* profiles, estimated via elastic superposition with the lighter lines connected to the loaded predecessors being paths of recovery. On unloading, some "shallowing-up" (≃6%) is ap-

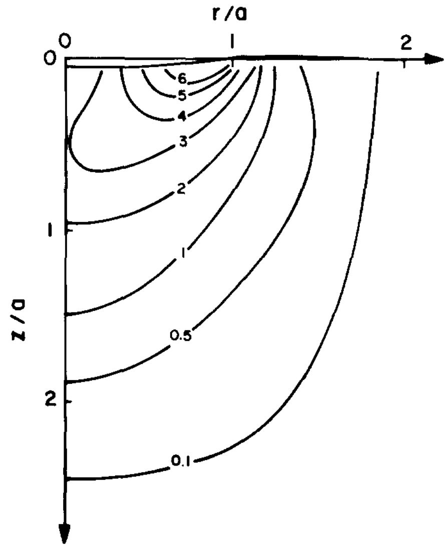

Fig. 9(a). Octahedral plastic strain contours with frictionless contact: early in the fully plastic regime (in %, $a/R = 0.13$).

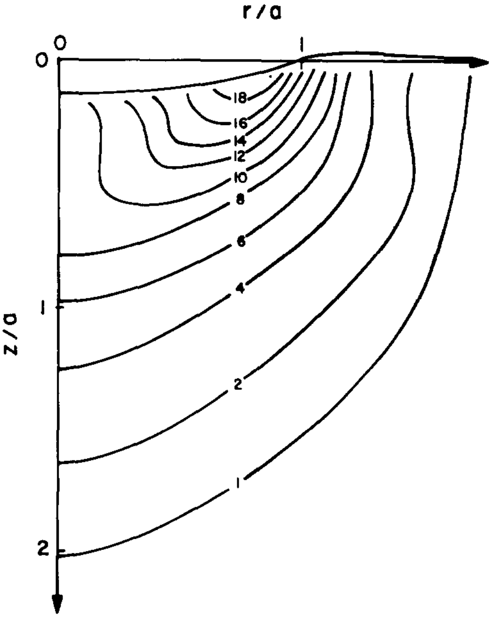

Fig. 9(b). Octahedral plastic strain contours with frictionless contact: late in the fully plastic regime (in %, $a/R = 0.32$).

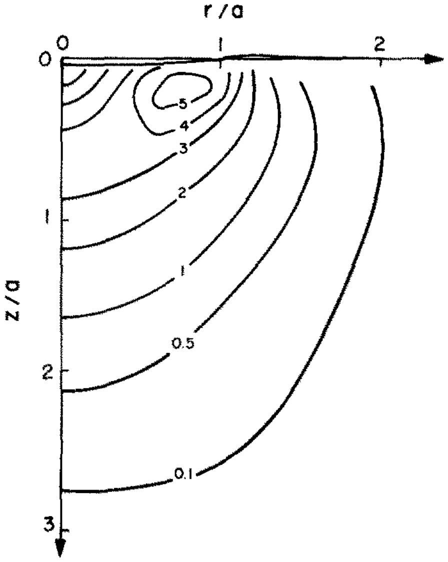

Fig. 10(a). Octahedral plastic strain contours with adhesive contact: early in the fully plastic regime (in %, $a/R = 0.13$).

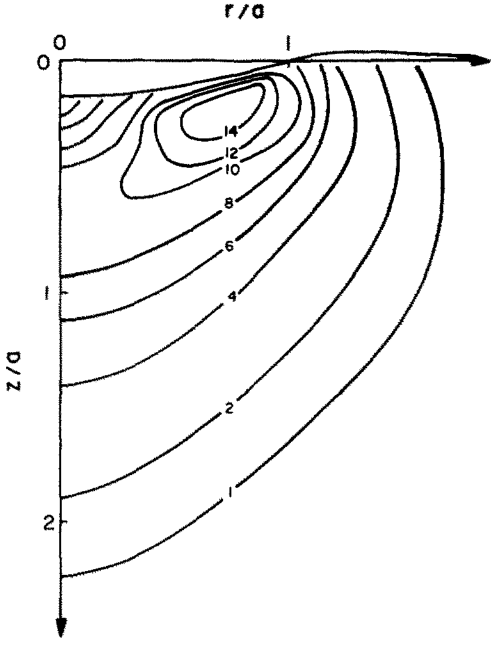

Fig. 10(b). Octahedral plastic strain contours with adhesive contact: late in the fully plastic regime (in %, $a/R = 0.32$).

parent in the depth of the impression but little if any effect on the diameter of the indentation is discernible. The distortion of the scales in Fig. 11 conceals the continued similarity of results in the fully plastic regime.

In all, it would seem that, for the overall indentation response, as well as the stresses and deformations induced in the configuration investigated, our finite element treatment within the theory of incremental elasto-plasticity furnishes useful estimates which are in reasonable agreement with the physical evidence: certainly, though, there remains room for improvement in analytical capability, both in the modeling of the physics and in the numerical analysis.

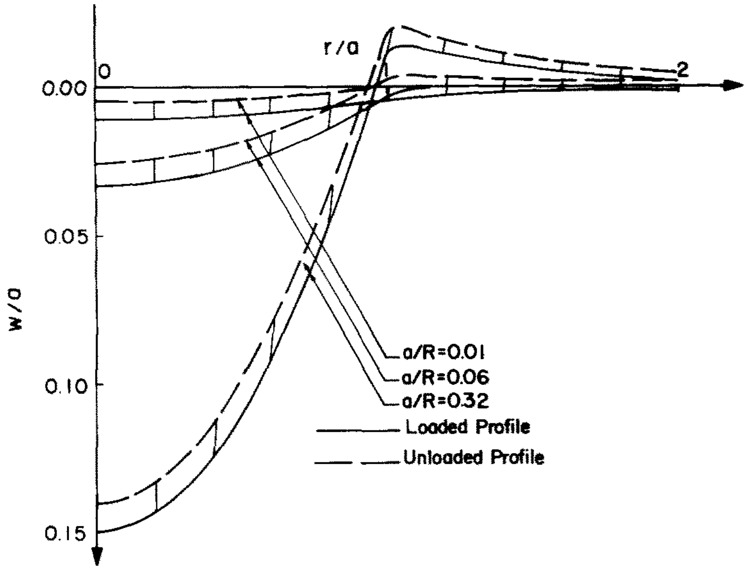

Fig. 11. Surface displacement profiles for frictionless contact.

Acknowledgements—We are pleased to extend our thanks to M. Mirdamadi for his assistance in carrying out the data reduction. The financial support of the Department of Energy, U.S.A., under grant number DE-AC02-79ER10468 is also appreciated.

REFERENCES

1. K. L. Johnson, Inelastic contact: plastic flow and shakedown. *Proc. Int. Symposium on Contact Mechanisms and Wear of Rail-Wheel Systems*, Vancouver (1982).
2. P. S. Follansbee and G. B. Sinclair, Quasi-static normal indentation of an elasto-plastic half-space by a rigid sphere—I. Analysis. *Int. J. Solids Structures* **13**, 81 (1984).
3. P. S. Follansbee, Mechanisms of erosive wear of ductile metals due to the low velocity, normal incidence, impact of spherical particles. Ph.D. Dissertation, Carnegie-Mellon University, Pittsburgh, PA (1981).
4. D. C. Ludwigson, Modified stress-strain relation for FCC metals and alloys. *Metall. Trans.* **2**, 2825 (1971).
5. D. Tabor, *The Hardness of Metals.* Oxford at the Clarendon Press (1951).
6. O. Richmond, H. L. Morrison, and M. L. Devenpeck, Sphere indentation with application to the Brinell hardness test. *Int. J. Mech. Sci.* **16**, 75 (1974).
7. A. J. Ishlinsky, The axi-symmetrical problem in plasticity and the Brinell test. *Prikl. Mat. Mekh* **8**, 233 (1944).
8. G. Eason and R. T. Shield, The plastic indentation of a semi-infinite solid by a perfectly rough circular punch. *Z. angew. Math. Phys.* **11**, 33 (1960).
9. R. T. Shield, On the plastic flow of metals under conditions of axial symmetry. *Proc. R. Soc.* (*Lond.*) **A233**, 267 (1955).
10. H. R. Hertz, *Miscellaneous Papers.* English transl., Macmillan and Co., London (1896).
11. K. L. Johnson, The correlation of indentation experiments. *J. Mech. Phys. Solids* **18**, 115 (1970).
12. H. T. Huber, Stresses in the contact of two elastic spheres. *Annls Phys.* **14**, 153 (1904).
13. H. A. Francis, Phenomenological analysis of plastic spherical indentation. *Trans. Am. Soc. mech. Engrs* **98**, *J. Engng Mater. Technology* 272 (1976).
14. C. Hardy, C. N. Baronet, and G. V. Tordion, The elasto-plastic indentation of a half-space by a rigid sphere. *Int. J. Num. Meth. Engng* **3**, 451 (1971).
15. C. H. Lee, S. Masaki, and S. Kobayashi, Analysis of ball indentation. *Int. J. Mech. Sci.* **14**, 417 (1972).
16. K. L. Johnson, An experimental determination of the contact stresses between plastically deformed cylinders and spheres. *Engineering Plasticity* 341, Cambridge University Press (1968).
17. A Cinar and G. B. Sinclair, Large indentation of an elastic half-space by an infinitely long rigid cylinder. Report SM 83-18, Dept. of Mechanical Engng., Carnegie-Mellon University, Pittsburgh, PA (1983).
18. K. L. Johnson, Reversed plastic flow during the unloading of a spherical indenter. *Nature* (Lond.) **199**, 1282 (1963).
19. A. E. H. Love, The stress produced in a semi-infinite solid by pressure on part of the boundary. *Phil. Trans. R. Soc.* (*Lond.*) **A228**, 377 (1929).
20. S. P. Timoshenko and J. N. Goodier, *Theory of Elasticity* 3rd Ed. McGraw-Hill, New York (1970).
21. C. J. Studman and J. E. Field, The indentation of hard metals: the role of residual stresses. *J. Mater. Sci.* **12**, 215 (1977).
22. J. O. Almen and P. H. Black, *Residual Stresses and Fatigue in Metals.* McGraw-Hill, New York (1963).
23. L. E. Samuels and T. O. Mulhearn, An experimental investigation of the deformed zone associated with indentation hardness impressions. *J. Mech. Phys. Solids* **5**, 125 (1957).
24. P. S. Follansbee, G. B. Sinclair, and J. C. Williams, Modelling of low velocity particulate erosion in ductile materials by spherical particles. *Wear* **74**, 107 (1981).

APPENDIX

Here we record the degree to which numerical noise is present in the results in Figs. 3–11, using the standard deviation s of (1.6) as a measure and noting the number of data points N used to calculate s (Table 2).

Table 2. Numerical noise levels in results presented

Source	Standard deviation and number of data points s	N	Comments
Fig. 3(b): frictionless	0.21 in ϵ(%)	6	*Cf.* $s = 2.8$ in ϵ for a straight line fit to Tabor's experimental results.
adhesive	0.23 in ϵ(%)	5	
Fig. 3(c): frictionless	0.03 in p/σ_f	6	
adhesive	0.05 in p/σ_f	5	
Fig. 4: present FEM for frictionless	0.09 in p/σ_f in fully plastic regime	9	$s = 0$ in the elastic regime and increases to this maximum value.
Fig. 5: $a/r = 0.01$	0.23 in σ_z/σ_f	10	Number of points varies because of FEM expansion technique.
$a/R = 0.06$	0.09 in σ_z/σ_f	13	
$a/R = 0.32$	0.17 in σ_z/σ_f	9	
Figs. 6: (a), all a/R	0.03 in σ_r/σ_f, σ_θ/σ_f	11-17	Values of s are the maximum occurring for the different load levels and stresses.
(b), all a/R	0.02 in σ_z/σ_f, σ_r/σ_f	9-11	
(c), (d), all a/R, frictionless	0.02 in σ_z/σ_f, σ_r/σ_f	10-14	
(c), (d), all a/R, adhesive	0.07 in σ_z/σ_f, σ_r/σ_f	10-14	
Fig. 7: all a/R	≤ 0.03 in σ_r/σ_f, σ_θ/σ_f, σ_z/σ_f	9-17	As for corresponding curve in Figs. 6.
Fig. 8	0.07 in ρ/a, ρ on elastic-plastic boundary	~20	Excluding elastic enclave boundary where $s = 0$.
Figs. 9, 10	—	—	Very similar noise levels to Fig. 8
Fig. 11: all a/R	0 in w/a	14-16	Lines shown pass through all points.